ACS Catalysis

Research Article

pubs.acs.org/acscatalysis

Understanding Pt Nanoparticle Anchoring on Graphene Supports through Surface Functionalization

Le Xin,[†] Fan Yang,[†] Somaye Rasouli,[‡] Yang Qiu,[§] Zhe-Fei Li,[†] Aytekin Uzunoglu,[#] Cheng-Jun Sun,[∥] Yuzi Liu,[⊥] Paulo Ferreira,[‡] Wenzhen Li,[§] Yang Ren,[∥] Lia A. Stanciu,[#,¶] and Jian Xie*[,†]

[†]Department of Mechanical Engineering, Purdue School of Engineering and Technology, Indiana University-Purdue University Indianapolis, Indianapolis, Indiana 46202, United States

[‡]Materials Science and Engineering Program, The University of Texas at Austin, Austin, Texas 78712, United States

[§]Department of Chemical and Biological Engineering, Biorenewables Research Laboratory, Iowa State University, Ames, Iowa 50011, United States

[#]School of Materials Engineering, Purdue University, West Lafayette, Indiana 47907, United States

[¶]Weldon School of Biomedical Engineering, Purdue University, West Lafayette, Indiana 47907, United States

[∥]Advanced Photon Source, Argonne National Laboratory, 9700 South Cass Avenue, Argonne, Illinois 60439, United States

[⊥]Center for Nanoscale Materials, Argonne National Laboratory, 9700 South Cass Avenue, Argonne, Illinois 60439, United States

ABSTRACT: The enhancement of Pt nanoparticle anchoring strength and dispersion on carbon supports is highly desirable in polymer electrolyte membrane fuel cells (PEMFCs) as well as in other catalysis processes. Presented here is a comprehensive study of the interaction between catalyst nanoparticles and carbon supports in terms of the electronic structure change and its effects on the electrocatalytic performance of supported catalysts. Graphene was chosen as an ideal model support because the unique 2-D structure allows the direct investigation of the interaction with supported metal nanoparticles at their interface. We developed a facile strategy to covalently graft *p*-phenyl SO_3H—or *p*-phenyl NH_2—groups onto the graphene surface. The functional groups were found to not only facilitate the homogeneous distribution of Pt nanoparticles on the surface of graphene supports and reduce the Pt average particle size but also strengthen the interaction of the Pt atoms with the functional groups and, consequently, minimize the migration/coalescence of the Pt nanoparticles in the course of accelerated durability tests. The experimental results from both X-ray photoelectron spectroscopy (XPS) and X-ray absorption spectroscopy (XAS) demonstrate the electron density shift from Pt to graphene supports with the strength of the Pt−graphene interaction following the trend of Pt/*p*-phenyl NH_2-graphene > Pt/*p*-phenyl SO_3H-graphene > Pt/graphene. This study will shed light on strategies to improve not only the durability but also the activity of the metal nanoparticles via the functionalization of the catalyst supports in the catalysis field.

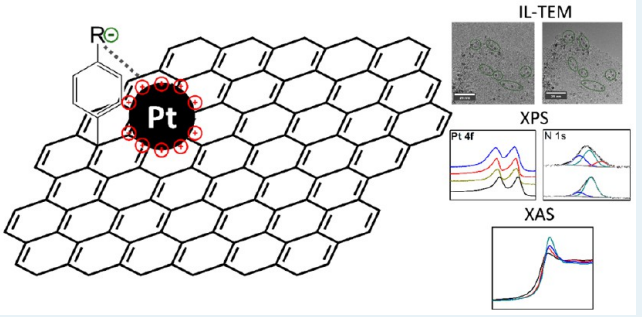

KEYWORDS: *surface functionalization, graphene, metal−support interaction, catalyst durability, oxygen reduction reaction, PEMFC*

1. INTRODUCTION

Polymer electrolyte membrane fuel cells (PEMFCs), which use hydrogen as the fuel and oxygen from the air to produce electricity, have attracted extensive interests over the past few decades.[1,2] Their high efficiency and zero emissions make PEMFCs promising candidates as power sources for both transportation and stationary applications.[3] Numerous experimental and theoretical studies have concentrated on developing highly efficient, low-cost electrocatalysts for oxygen reduction reactions (ORRs) by alloying Pt with secondary elements,[4] dealloying Pt−M binary alloys,[5] or synthesizing the core−shell structure with Pt overlayers.[5a,6] These studies have led to a considerably lower usage of Pt while boosting ORR activity. However, catalyst stability on support materials still remains one of the major challenges that hinder the widespread commercialization of PEMFCs.[7] The durability of electrocatalysts requires that they maintain the beginning of life (BOL) activity over long-term operations of PEMFCs. As this is realized, the overall cost of PEMFCs could be further reduced. Shrinking Pt particle sizes into the nanoscale (2−3 nm) followed by dispersing the Pt nanoparticles well on carbon supports has great benefits for increasing the surface area and the utilization of Pt, making Pt-based catalysts more active.[8] However, these Pt nanoparticles have a high surface energy that

Received: November 30, 2015
Revised: February 9, 2016
Published: March 11, 2016

DOI: 10.1021/acscatal.5b02722
ACS Catal. 2016, 6, 2642−2653

is thermodynamically unstable, and they tend to grow into larger particles during long-term PEMFC operation following two proposed mechanisms: i.e., Pt dissolution and redeposition (Ostward ripening) and Pt migration and coalescence.[9] Although there has been a debate for quite a long time on which is the dominant process, the root cause of the performance degradation (in general) lies in the weak anchoring of the Pt nanoparticles over the carbon surface, which causes a weak interaction between the Pt nanoparticles and carbon supports. To solve this issue, several recent studies have focused on developing methods to immobilize the Pt nanoparticles, including the introduction of conductive polymers (polyaniline (PANI),[10] pyridine-containing polybenzimidazole (PyPBI),[11] and polybenzimidazoles (PBIs)[12]) that were coated on carbon nanotubes (CNTs) or graphene, embedding Pt nanoparticles on nitrogen- or sulfide-doped CNTs or graphene,[13] or synthesizing hybrid functional graphene that involves metal oxide (i.e., indium tin oxide (ITO)) to create metal−metal oxide−graphene triple junctions.[14] These modifications made on different carbon supports not only provide binding sites to stabilize the Pt particles but also affect the Pt electronic structure that promotes catalytic activity for the ORR.

The binding of metal nanoparticles on the surface of supports with different properties is a widespread topic in heterogeneous catalysis, which has a profound influence on the electronic structure of the supported metal catalysts, thereby greatly affecting the catalytic activity and stability.[15−19] Hence, a fundamental understanding of metal−support interactions will provide insights into the rational design of efficient catalyst systems that will have a huge economic impact in vast industrial sectors (i.e., the petroleum, chemical, and fertilizer industries). Pt supported on different materials (i.e., ceramics, metal oxides, and carbon black) has found very wide applications in catalysis. The stable binding of Pt nanoparticles onto supports is of paramount significance for long-term performance: namely, durability. However, studying the interactions between Pt nanoparticles and the support materials of disordered architectures is rather difficult because of the inhomogeneous surface morphology and chemical properties of the support materials.

Graphene is a single layer of sp^2-hybridized carbon atoms arranged in a honeycomb crystal structure and can be viewed as an individual atomic plane of the graphite structure.[20−23] The 2-D carbon network of flat basal planes makes graphene an ideal model support that allows close observation of the metal nanoparticle morphology and direct study of the metal−support interactions. In this study, Pt nanoparticles were deposited on three different graphene supports. Unmodified graphene was prepared via the chemical exfoliation of graphite followed by the reduction of graphene oxide according to a modified Hummers method.[24] Graphene surface functionalization was carried out by covalently grafting *p*-phenyl SO_3H− or *p*-phenyl NH_2− groups on the $\pi-\pi$ conjugated honeycomb carbon network, which is expected to tailor the chemical properties of the graphene surface to make it more uniform. The morphological changes of the Pt nanoparticles on different supports that were subject to potential cycling in 0.1 M $HClO_4$ could be directly visualized using identical location transmission electron microscopy (IL-TEM). Insights into the effects of electron delocalization induced by *p*-phenyl SO_3H− and *p*-phenyl NH_2− groups on top-layer Pt atoms of Pt nanoparticles were further studied using both X-ray photoelectron spectroscopy (XPS) and X-ray absorption spectroscopy (XAS). The Pt−graphene support interaction investigated by these advanced spectroscopic techniques uncovered the possible orientation of Pt nanoparticles with different functional groups, which was then correlated with their durability performance. The comprehensive study presented in this work on the interaction between Pt and its underlying graphene supports and the strategies for strengthening the Pt−C interaction can be extended to stabilize the supported metal nanocrystal catalysts in the catalysis community.

2. EXPERIMENTAL SECTION

2.1. Surface Functionalization of Graphenes. Graphene oxide (GO) was prepared following a modified Hummers method.[24,25] Before the diazonium reaction, GO was prereduced by adding $NaBH_4$ to a 100 mL GO aqueous dispersion (1 mg/mL) to partially recover the sp^2 carbons. The mixture was then heated to 80 °C and held for 1 h. The mildly reduced graphene oxide (mrGO) was collected by centrifuge and washed with DI water several times. For the synthesis of *p*-phenyl SO_3H−graphene (abbreviated as SO_3H-graphene hereafter), mrGO was redispersed in DI water, followed by the addition of sulfanilic acid, concentrated H_2SO_4, and sodium nitrite ($NaNO_2$) in a molar ratio of 1:1:1. Subsequently, the mixture was kept at 60 °C for 4 h. After centrifuging and rinsing with DI water/ethanol several times, the obtained SO_3H-mrGO was redispersed in DI water. Hydrazine was then added to the dispersion, and the reaction mixture was refluxed at 100 °C overnight with constant stirring, yielding SO_3H-graphene. The preparation of *p*-phenyl NH_2−graphene (abbreviated as NH_2-graphene hereafter) follows similar procedures (as illustrated in Scheme 1), except that *p*-phenylenediamine and concentrated HNO_3 were used instead of sulfanilic acid and concentrated H_2SO_4, respectively.

Scheme 1. Procedures of Diazonium Reactions for Covalent Functionalization of the Graphene Surface

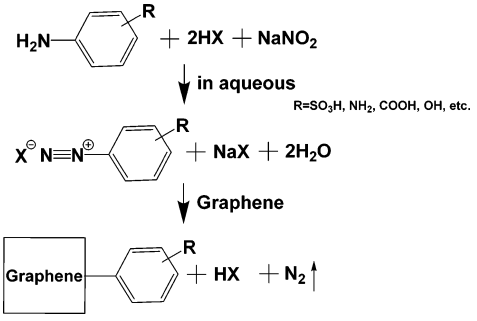

2.2. Loading the Pt Catalyst on Supporting Materials. Pt nanoparticles were loaded on functional graphene in an aqueous ethylene glycol (EG) solution (EG/water 3/2 v/v). First, NH_2-graphene or SO_3H-graphene was added to an EG aqueous solution, and the dispersion was sonicated for 30 min, followed by the quick addition of an aqueous EG solution of $H_2PtCl_6{\cdot}6H_2O$. After the mixture was refluxed at 140 °C for 6 h, the solid materials were collected by filtration and washed with copious amounts of DI water and ethanol. The obtained solid (Pt/NH_2-graphene or Pt/SO_3H-graphene) was dried in a vacuum oven. For comparison, Pt/graphene was prepared by the same procedures using unmodified graphene instead of NH_2- or SO_3H-graphene.

DOI: 10.1021/acscatal.5b02722
ACS Catal. 2016, 6, 2642−2653

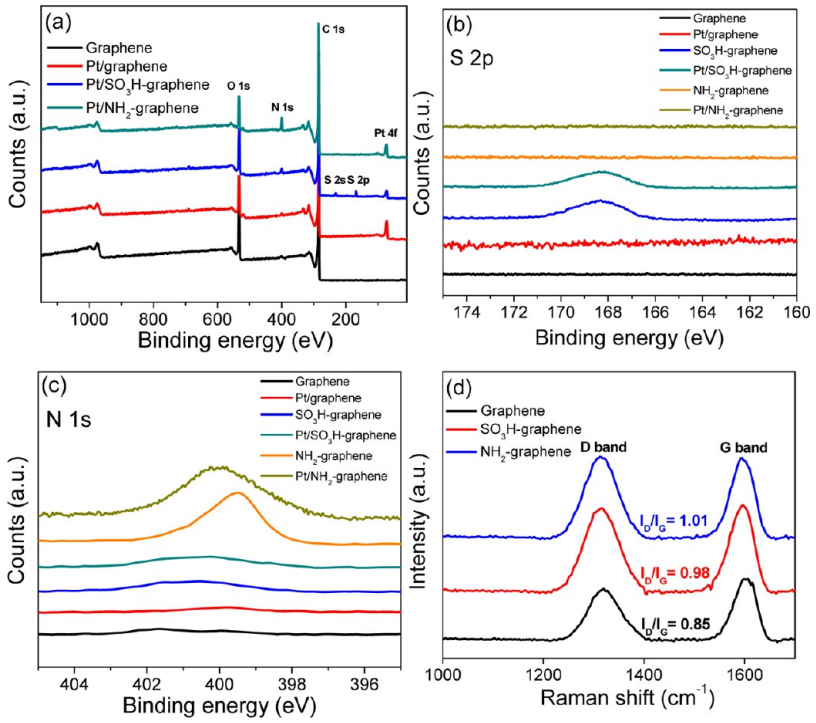

Figure 1. (a) Wide survey XPS spectra of graphene, SO_3H-graphene, and NH_2-graphene supported Pt nanoparticles. High-resolution XPS spectra of (b) S 2p and (c) N 1s of different supports before and after Pt nanoparticle deposition. (d) Raman spectra of graphene, SO_3H-graphene, and NH_2-graphene.

2.3. Physical Characterizations. The morphology of all catalysts was characterized by a JEOL JEM-2100F transmission electron microscope (TEM) operated at 200 kV. The particle size distribution was obtained on the basis of random measurements of more than 200 primary Pt nanoparticles, excluding the agglomerations in TEM images. Raman spectra were taken with a Craic Tech spectrometer with laser excitation at 785 nm. X-ray photoelectron spectroscopy (XPS) was carried out on a Kratos Amicus/ESCA 3400 instrument with Mg Kα X-rays (1253.6 eV). The XPS instrument was calibrated with the Cu 2p3/2 peak at 932.66 eV and Cu 3p peak at 75.13 eV. All spectra were calibrated with the C 1s peak at 284.6 eV. The X-ray absorption near edge structure (XANES) measurements were carried out at beamline 20BM-B of the Advanced Photon Source (APS), Argonne National Laboratory. The energy of the beam was calibrated with the first derivative point of standard XANES for Pt L_{III} edge (E = 11.564 keV). The sample was prepared using a cylindrical die under the pressure of a compressing machine to form a round plate and was sealed between two pieces of Kapton tape. The obtained sample was then assembled on the sample holder, which was then fixed on the beamline. The measurement was conducted under the transmission mode of a high-energy X-ray, and the data were analyzed by the Athena software package.

The setup of the identical location TEM (IL-TEM) was developed to simulate the effects of voltage cycling on the cathode catalysts in fuel cells.[26−28] For this purpose, the catalyst powder was deposited on a gold TEM grid attached to a gold plate, which was employed as a working electrode in a three-electrode electrochemical cell. The TEM grids were then cycled between 0.6 and 1.0 V (vs hydrogen reduction potential reversible hydrogen electrode (RHE)) in 0.1 $HClO_4$ liquid electrolyte for 1000 cycles. In this fashion, predefined locations of the electrocatalyst on the TEM grid were analyzed before and after cycling.

2.4. Electrochemical Characterizations. Electrochemical measurements were performed in a three-electrode electrochemical cell using a glassy-carbon rotating disk electrode (RDE) (0.196 cm^2, Pine Instruments) as the working electrode. This electrode was polished with a 0.3 μm alumina suspension followed by a 0.05 μm alumina suspension until a mirrorlike finish was obtained. To prepare the catalyst ink, the prepared catalyst was suspended by sonication in an isopropyl alcohol/DI water mixture (1/4 v/v) with a 20 wt % Nafion solution (5 wt %, Ion Power, Inc.). A 10 μL Pt suspension was dropped onto the glassy-carbon electrode and dried. The mass loading of Pt was estimated to be 3.4 $\mu g/cm^2$. A Pt wire (Pine Instruments) served as the counter electrode, and a reversible hydrogen electrode (RHE, HydroFlex) was used as the reference electrode. Electrochemical experiments were performed using an electrochemical potentiostat (VSP, Biologic, TN). All potentials cited in this work were normalized with respect to the RHE. Prior to the electrochemical tests, the catalysts were electrochemically cleaned by cycling the potential between 0.05 and 1.20 V (vs RHE) at 500 mV/s for 100 cycles in a N_2-saturated 0.1 M $HClO_4$ electrolyte. Cyclic voltammetry (CV) scanning from 0.05 to 1.00 V (vs RHE) at a 50 mV/s scan rate was then carried out for ECSA measurements. Polarization curves of the ORRs on an RDE were recorded by linearly sweeping the potential from 0.20 to 1.20 V (vs RHE) at a 20 mV/s scan rate in an O_2-saturated 0.1 M $HClO_4$ aqueous solution with a rotating speed of 1600 rpm. All mass activities were calculated on the basis of the mass transport corrected kinetic current at a potential of 0.90 V (vs RHE) according to the Levich−Koutecky equation[29] and normalized by the mass loading of Pt on the RDE. The specific activities were calculated by normalizing kinetic current by ECSA. Accelerated

DOI: 10.1021/acscatal.5b02722
ACS Catal. 2016, 6, 2642−2653

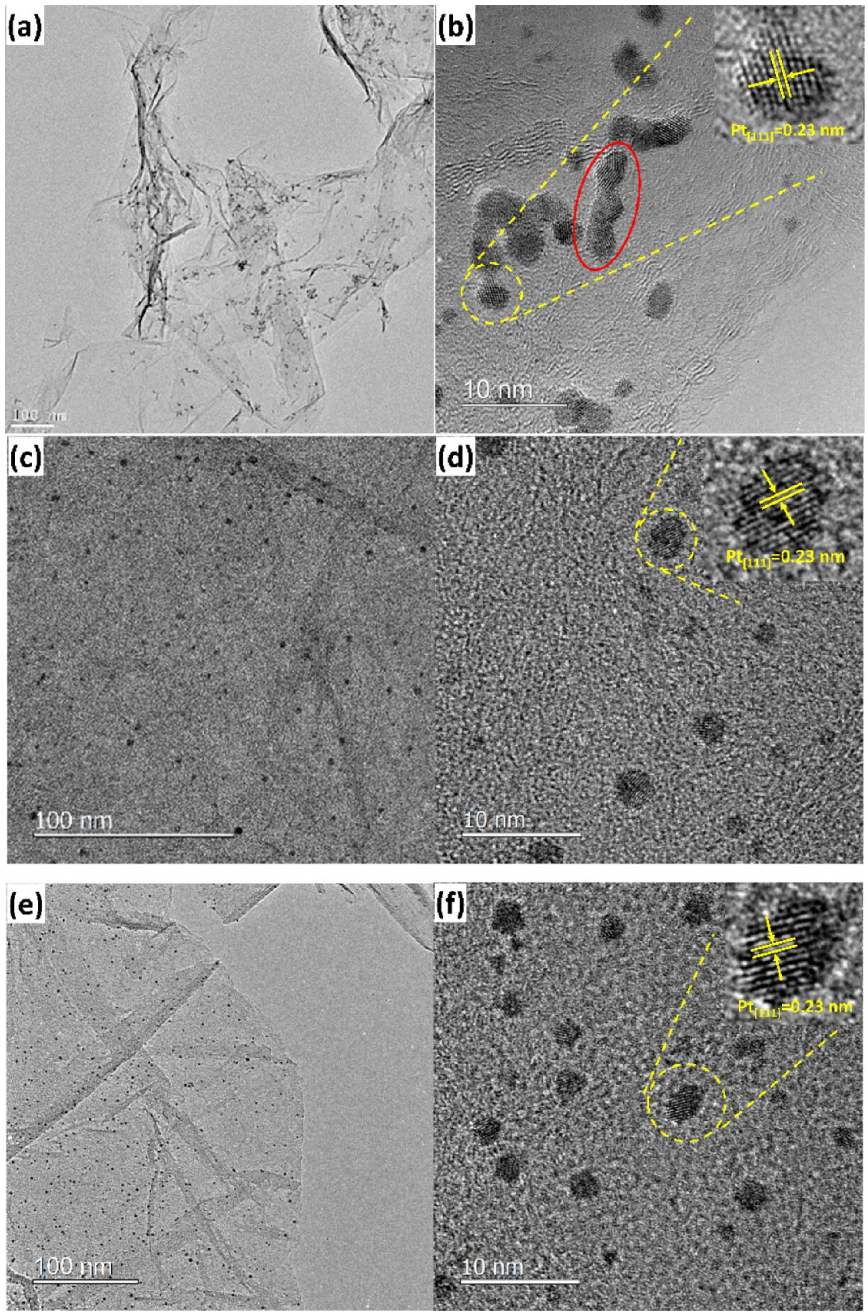

Figure 2. TEM micrographs of Pt nanoparticles supported on (a, b) graphene, (c, d) SO_3H-graphene, and (e, f) NH_2-graphene with a loading of 10 wt %. The rodlike structure of the Pt particles on graphene is circled in (b).

degradation tests (ADT) were performed by potential scanning between 0.6 and 1.0 V (vs RHE) at a scan rate of 100 mV/s in the 0.1 M $HClO_4$ that was exposed to the atmosphere for 20000 cycles, followed by the recording of electrochemical surface area (ECSA), mass activity, and specific activity loss.

3. RESULTS AND DISCUSSION

The surface functionalization of graphene by *p*-benzensulfonic acid or *p*-benzeneamino groups was achieved by a modified diazonium reaction where in situ generated aryldiazonium salt was covalently grafted onto the graphene surface.[30] A wide survey of the XPS spectra (Figure 1a) clearly shows that, in addition to C 1s (284.9 eV) and O 1s (531.9 eV), N 1s (399.9 eV) and S 2s (231.9 eV) and S 2p (168.0 eV) appear on NH_2-graphene and SO_3H-graphene, respectively, which indicates the successful incorporation of either the *p*-phenyl SO_3H- or the *p*-phenyl NH_2- onto the surface of the graphene sheets. It is also shown in high-resolution XPS spectra that S 2p signals were absent for those samples that did not undergo surface functionalization with *p*-benzenesulfonic acid (S-containing group) (Figure 1b). However, there exist N 1s peaks around 400 eV on graphene and SO_3H-graphene before and after Pt nanoparticle deposition, although they are much smaller in comparison with NH_2-graphene and Pt/NH_2-graphene (Figure 1c). These N 1s spectra can be assigned to pyrazole groups on the edge of reduced graphene oxide that was treated with the reducing agent hydrazine during the synthesis.[31] The surface concentrations of nitrogen on NH_2-graphene and of sulfur on SO_3H-graphene are 5.7 and 1.3 atom %, respectively, which are

DOI: 10.1021/acscatal.5b02722
ACS Catal. 2016, 6, 2642−2653

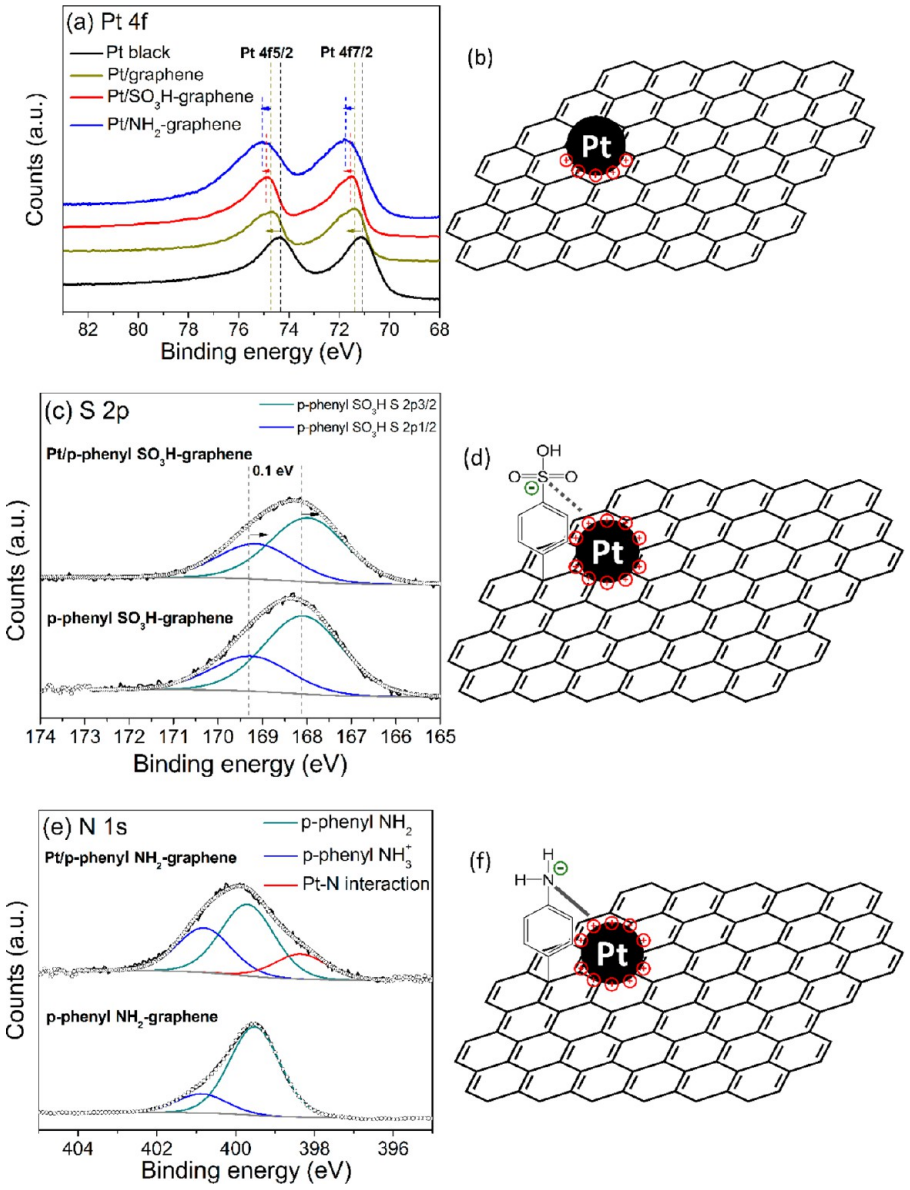

Figure 3. High-resolution XPS spectra of (a) Pt 4f, (c) S 2p, and (e) N 1s. The possible configurations of the interaction between Pt nanoparticles and functional graphenes are illustrated in (b), (d), and (f), where dotted lines and solid lines illustrate the weak S−Pt and strong N−Pt interactions, respectively.

estimated according to the peak area corrected by the relative sensitivity factor. The structural defects of graphene induced by covalently bonding functional groups has been confirmed by Raman spectroscopy (Figure 1d). The Raman spectra for graphene, SO_3H-graphene, and NH_2-graphene display two characteristic absorption bands (the D band and the G band), which are associated with the defects or disorders and the sp^2-bonded carbons in graphitic carbon based materials, respectively.[32,33] The intensity ratio of the D band and the G band (I_D/I_G) is usually employed to estimate the number of defects in graphitic materials.[34,35] The increase in the I_D/I_G value from 0.85 for graphene to 0.98 for SO_3H-graphene and 1.01 for NH_2-graphene suggests the covalent bonding of aryl molecules that leads to the disruption of sp^2 carbons in the graphene sheets and the increase of sp^3-hybridized carbons.[36]

Pt nanoparticles were then loaded on these supports using the wet chemistry method.[12b,30b] First, 1.0 mM chloroplatinic acid (H_2PtCl_6) was mixed well with the graphene supports in aqueous solution containing the EG reagent, during which sufficient time was allowed for better contact between the Pt precursor (H_2PtCl_6) and the different graphene supports. In this step, platinum complex ions (i.e., $PtCl_6^{2-}$) from the solution land on the surface of the graphene sheets, following the formation of a group/pack of ions or ion clusters. Depending on the surface chemistry of the graphene, the Pt complex ions may distribute randomly if the graphene surface is chemically clean. On the other hand, these Pt complex ions may be preferentially attracted by charged functional groups or defect sites if present on the graphene surface. Either an ionic bond or a covalent bond may be formed between the Pt complex ions and the charged functional groups or the defective carbons. This bond guides the distribution of the Pt ion clusters.

Subsequently, the temperature of the solution was gradually increased and the reduction of the Pt precursor started to take place in the presence of a mild reducing agent of EG. During

DOI: 10.1021/acscatal.5b02722
ACS Catal. 2016, 6, 2642−2653

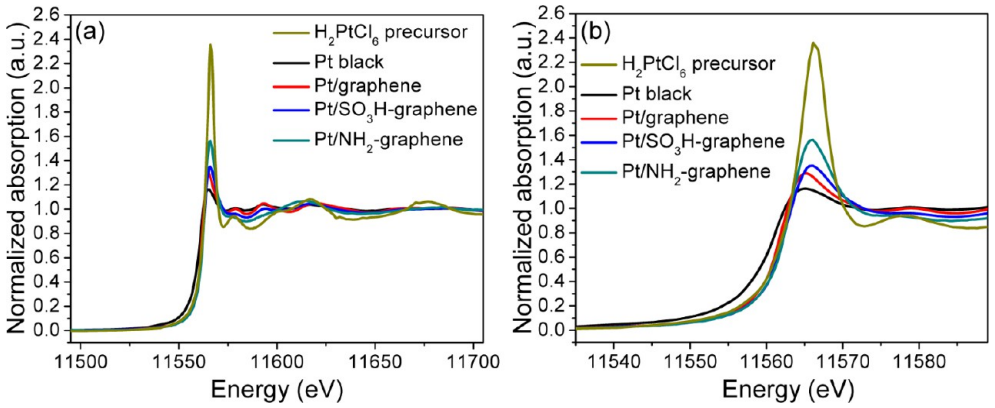

Figure 4. Pt L_{III}-edge XANES spectra of H_2PtCl_6 precursor, Pt black, Pt/graphene, Pt/SO_3H-graphene, and Pt/NH_2-graphene.

this step, some of the Pt complex ions are nucleated. These initially formed Pt atoms then serve as the nuclei where other Pt ions in the ion clusters are further reduced to Pt atoms. Those Pt atoms pack around the initially formed Pt nuclei following a crystalline structure. After the Pt complex ions land, the deposition of Pt nanoparticles depends on the surface chemistry of the graphene support. For unmodified graphene, Pt nanoparticles prefer the edge and folded area (i.e., where two or more layers of graphene sheets fold to form wrinkles) where the defects are populated (Figure 2a).[37] On the graphene basal plane, its inertness and hydrophobicity do not accommodate facile Pt deposition, leading to a smaller number of Pt nanoparticles.[38] In addition, once the Pt complex ions ($PtCl_6^{2-}$) are reduced to Pt metal atoms, their interaction with the unmodified graphene could be weakened, becoming a van der Waals bond. Therefore, freshly formed Pt nuclei tended to diffuse on the graphene surface, resulting in the "rod-like" aggregates, as highlighted by the red circle in Figure 2b. In sharp contrast, the SO_3H- and NH_2- functional groups that were covalently bonded to the graphene provided anchoring sites across the entire graphene plane that enabled the homogeneous landing of the Pt complex ions. The uniformly distributed Pt nanoparticles over the functionalized graphene sheets also suggests that these SO_3H- and NH_2- functional groups were uniformly covalently bonded over the entire graphene sheet. After steady nucleation and growth, Pt nanoparticles were then uniformly distributed on both the edge and the basal regions of the graphene sheets that mostly exhibit a "sphere-like" morphology with fewer aggregations (Figure 2c–f). The lattice fringes of high-resolution TEM (HRTEM) images (Figure 2b,d,f, inset) illustrate the good crystallinity of the Pt nanoparticles on graphene, SO_3H-graphene, and NH_2-graphene. The measured lattice space is 0.23 nm, corresponding to the (111) planes of the face-centered cubic (*fcc*) Pt crystals.

The interaction between the Pt nanoparticles and the graphene supports was then evaluated using XPS and XAS. In order to minimize the interference of the Pt–Pt interaction with the analysis of the interaction between the Pt and functional graphene and to enhance the signals of the Pt–C interaction by increasing the number of Pt atoms in direct contact with C atoms, a loading of Pt of 10 wt % on different supports was employed so that smaller Pt nanoparticles could form (the smaller the radius of a particle, the higher the number of atoms on the outermost surface of the particle). Figure 3a shows the high-resolution Pt 4f XPS spectra where both of the Pt $4f_{5/2}$ and Pt $4f_{7/2}$ peaks in Pt black shift 0.28 eV to higher binding energy as the Pt is deposited on the graphene, which indicates that there exists a strong interaction between the Pt and graphene carbon matrix, leading to an electron density shift from the Pt to the graphene supports (Figure 3b). When the Pt landed on the SO_3H-graphene and the NH_2-graphene, it is interesting to note a further positive shift of the Pt 4f binding energy (by 0.21 and 0.37 eV, respectively) related to the Pt/graphene. These additional shifts to higher binding energies as a result of the graphene surface functionalization reveal that the functional groups have promoted an electron density shift from Pt atoms of Pt nanoparticles to SO_3H-graphene and NH_2-graphene, respectively. The cause of this strengthened electronic interaction could have two possibilities: (1) the modification of the graphene surface could tune the chemical environment at the interface between the bottom layers of the Pt atoms and the supporting carbons or (2) the S and N present in the functional groups could interact with the top layers of the Pt atoms.[13c,10b,13a] Figure 3c shows that both SO_3H-graphene and the Pt/SO_3H-graphene exhibit characteristic S 2p peaks, centered at ca. 168.0 eV, which is due to the presence of sulfonate sulfur (R-SO_3H).[39] This S 2p band can be deconvoluted into a pair of superimposed S 2p1/2 and S 2p3/2 doublets, with their respective locations at 169.3 and 168.1 eV for SO_3H-graphene and at 169.2 and 168.0 eV for Pt/SO_3H-graphene. The negative shift of S 2p spectra by 0.1 eV on Pt/SO_3H-graphene (Figure 3c) correlates with the positive shift of Pt 4f spectra in comparison with Pt/graphene (Figure 3a), which confirms the electronic arrangement of (δ^+)Pt-(δ^-)-SO_3H-graphene resulting from the electron density shift between Pt and S (Figure 3d). On the other hand, a high-resolution N 1s spectrum was collected in order to elucidate the different chemical environments of nitrogen in NH_2-graphene and Pt/NH_2-graphene, as shown in Figure 3e. The fitted N 1s peaks for NH_2-graphene centered at 399.5 and 400.9 eV are attributed to *p*-phenyl amine ($-NH_2$) and protonated *p*-phenyl ammonium ion ($-NH_3^+$), respectively.[10b,40] In addition to these two types of nitrogens, an extra deconvoluted N 1s peak was positioned at 398.3 eV on Pt/NH_2-graphene due to the presence of a Pt–N bond between the surface Pt atoms of the Pt nanoparticles and the N atoms on the *p*-phenyl NH_2- functional group.[41] The N 1s spectra results correlate well with a greater increase in the Pt 4f binding energy observed on the Pt/NH_2-graphene, in comparison with that on the Pt/graphene, which asserts the enhanced interaction between Pt and NH_2-graphene. It is also worth speculating that NH_2-

DOI: 10.1021/acscatal.5b02722
ACS Catal. 2016, 6, 2642–2653

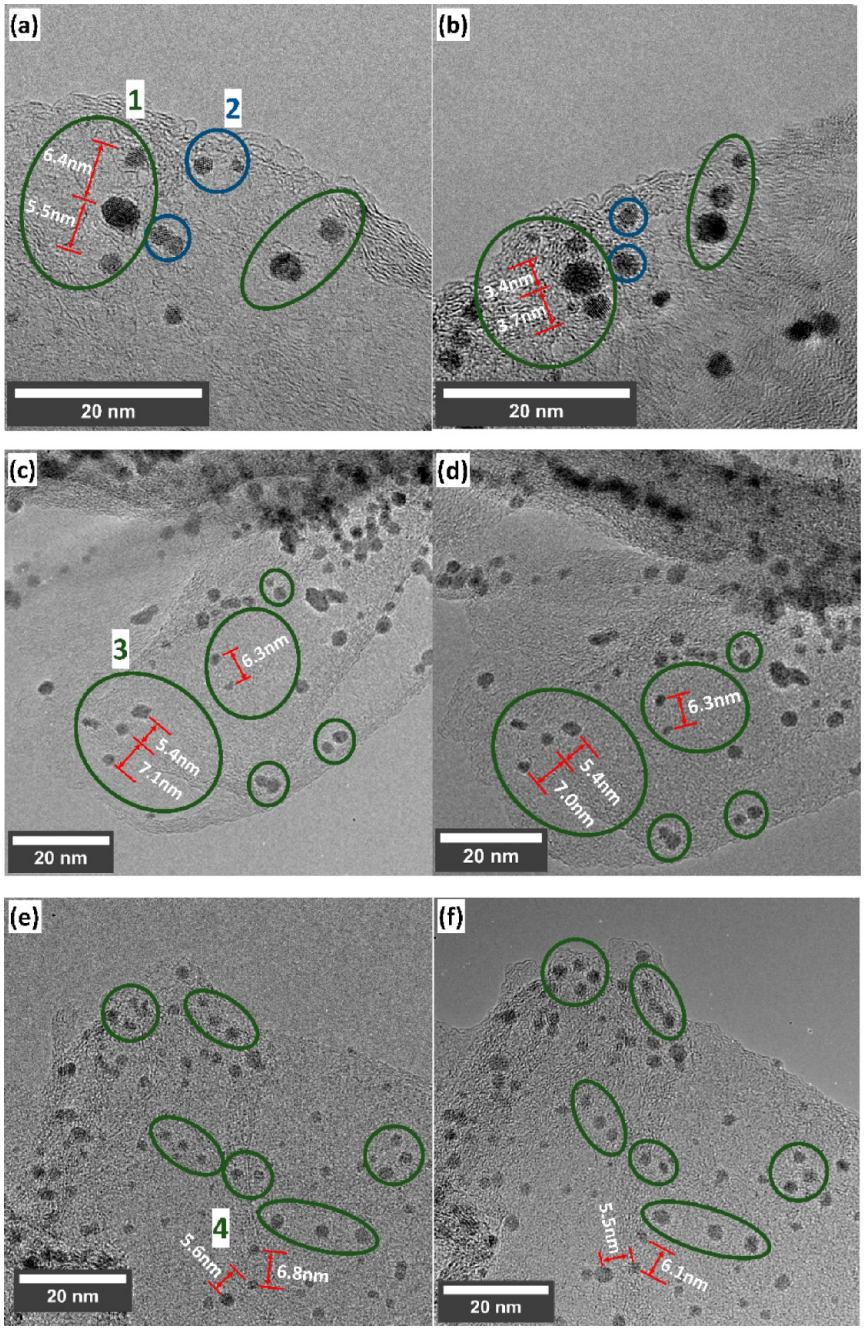

Figure 5. IL-TEM micrographs of (a, b) graphene, (c, d) SO_3H, and (e, f) NH_2 graphene supported Pt nanoparticles (10 wt %) before and after potential cycling from 0.6 to 1.0 V vs RHE in 0.1 M $HClO_4$ for 1000 cycles. Green circles indicate the change in the relative distance of separated Pt particles; blue circles show the reshaping of the Pt nanoparticles due to their agglomerations.

graphene delocalizes the electron density toward N atoms from the neighboring Pt atoms to a greater extent than the formation of the Pt−N bond (at 398.3 eV) (Figure 3f), whereas the Pt−S bond is absent in the S 2p spectra of Pt/SO_3H-graphene, suggesting that the SO_3H-graphene interacts relatively weakly with the surface Pt atoms of the Pt nanoparticles (Figure 3d). Even though XPS results clearly confirm that interactions exist between the surface atoms of Pt nanoparticles and S or N species on *p*-phenyl SO_3H− and *p*-phenyl NH_2− functional groups, the possible bonding between the Pt and C atoms cannot be ruled out. The C 1s XPS spectra were analyzed, but a clear interaction between the C atoms from the graphene surface and the Pt atoms from the Pt nanoparticles over graphene sheets could not be concluded, since the complexity of the chemical/electronic nature of carbon atoms on the functional graphene compromises the accuracy of the results from the C 1s XPS study. Work on the Pt−C interaction is ongoing and will be reported later. Nevertheless, on the basis of the XPS results, it can be concluded that the Pt atoms prefer to nucleate close to these regions on the graphene sheets where *p*-phenyl SO_3H− or *p*-phenyl NH_2− was covalently grafted and S or N atoms of functional groups enhanced the stability of the Pt nanoparticles through weak bonding with the surface Pt atoms.

This interesting phenomenon was further investigated using XAS. The normalized XANES spectra for the Pt L_3 edge are shown in Figure 4a, measured at the beamline 20-BM-B of the

DOI: 10.1021/acscatal.5b02722
ACS Catal. 2016, 6, 2642−2653

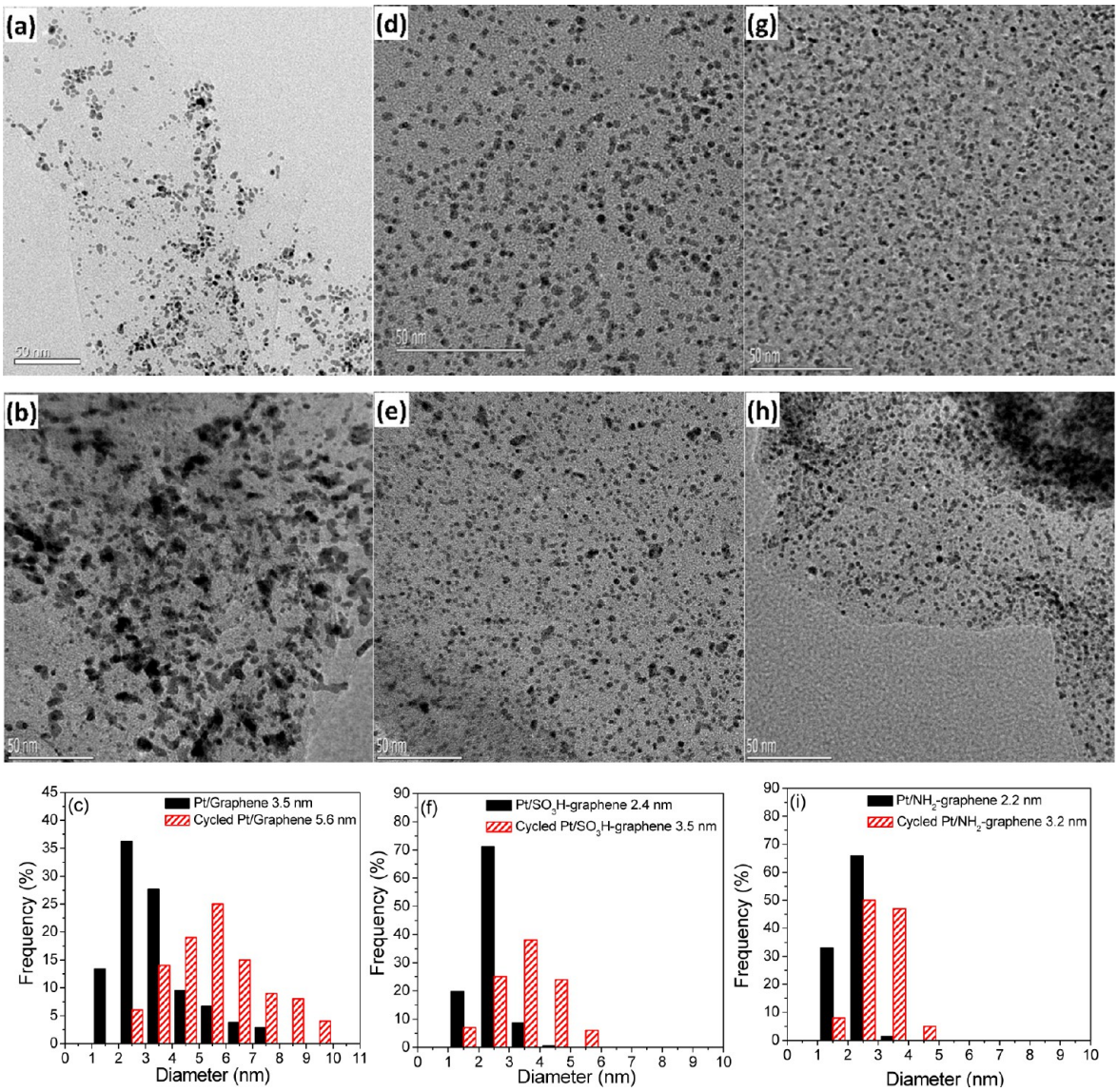

Figure 6. TEMs and particle size histograms of (a–c) Pt/graphene, (d–f) Pt/SO_3H-graphene, and (g–i) Pt/NH_2-graphene before and after 20000 cycles of ADT.

Advanced Photon Source (APS) at Argonne National Laboratory. Strong peaks of the white line (WL) appear in the XANES region (Figure 4a), indicating that the dipole allowed a photoelectron transition from the 2p core to the unoccupied 5d state.[42,43] The WL intensity is regarded to be proportional to the empty electron density in the Pt 5d orbital.[44,45] The L_3-edge absorption resonance of Pt^{4+} in the H_2PtCl_6 precursor is rather intense due to its greater number of vacancies in the Pt 5d states. Successful reduction of H_2PtCl_6 to metallic Pt, as shown in Figure 4b for Pt black, was revealed by a decrease in the absorption intensity as well as a shift of the absorption threshold to a lower energy value. When graphene was used to support Pt, the intensity of the L_3-edge absorption increased, because of the effects of the Pt–graphene interaction on the unoccupied 5d state of the supported Pt (Figure 4b). However, for Pt supported on functionalized graphene, the electron density shift from Pt to SO_3H-graphene or NH_2-graphene led to a higher vacancy of the Pt 5d state, as reflected in the further increase in the absorption intensity of the Pt L_3-edge spectra (Figure 4b). The stronger the interaction of the Pt and graphene support, the higher the intensity of the L_3-edge absorption, which reveals the following order of Pt–graphene support interaction strength: Pt/NH_2-graphene > Pt/SO_3H-graphene > Pt/graphene. On the other hand, Figure 4b also shows that the photon energy of the Pt L-edge absorption peak shifts from 11565.3 eV for Pt/graphene to 11566.1 eV for both Pt/SO_3H-graphene and Pt/NH_2-graphene. The increase of the absorption energy by 0.8 eV justifies the possibly slight increase of the oxidation state of Pt caused by the electron density shift from Pt to functional graphene as a result of their enhanced interaction. The XAS results are in very good agreement with the XPS studies, as shown in Figure 3. These results clearly indicate that functional graphene (SO_3H-graphene or NH_2-graphene) influences the valence electrons of Pt atoms and is expected to play an important role in the stability of Pt nanoparticles in catalysis applications.

The effects of the functional groups (SO_3H– and NH_2–) on the mobility of the Pt nanoparticles over graphene during electrochemical treatments were investigated using IL-TEM. A gold-coated carbon grid with the appropriate coordinates was

DOI: 10.1021/acscatal.5b02722
ACS Catal. 2016, 6, 2642–2653

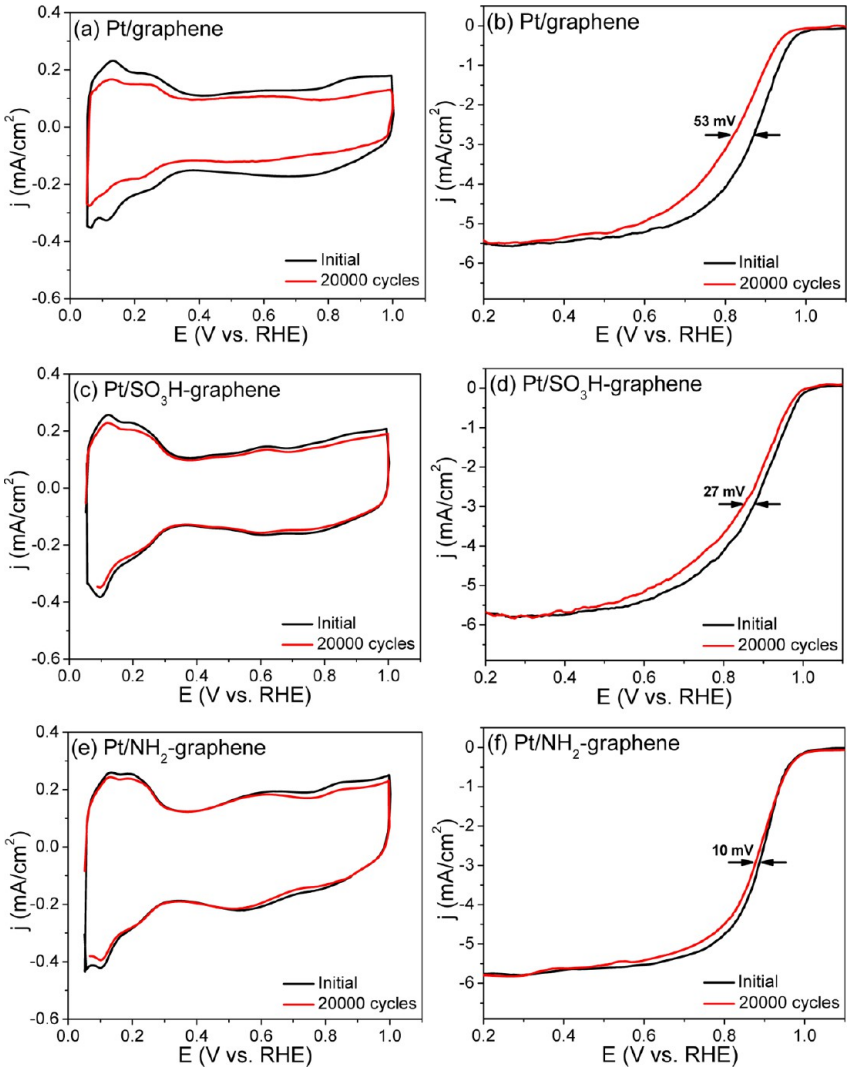

Figure 7. (a, c, e) CV curves and (b, d, f) ORR polarization curves of Pt/graphene, Pt/SO_3H-graphene, and Pt/NH_2-graphene with 30 wt % loading of Pt nanoparticles before (black) and after (red) 20000 cycles of ADTs.

used as the working electrode in a three-electrode cell. This method helps locate the same area to track the individual particles before and after the potential cycling from 0.6 to 1.0 V vs RHE in 0.1 M $HClO_4$ for 1000 cycles. IL-TEMs were taken at several locations, and representative images at high magnifications are presented in Figure 5. When parts a and b of Figure 5 are compared, the migration of the Pt nanoparticles on the graphene sheets without functionalization is evident. The green circles highlight the regions where changes can be observed between the selected Pt nanoparticles as the Pt/graphene is subjected to potential cycling. For example, in location 1, three initially separated Pt particles came into contact with each other after potential cycling, and the interparticle distances were reduced from 6.4 and 5.5 nm to 3.4 and 3.7 nm, respectively. In location 2 (blue circles), two individual particles, with sizes of 1.7 and 0.8 nm, respectively, became one single larger particle of 2.5 nm, which is the more direct evidence of the agglomeration. The main cause of this phenomenon can be attributed to the weak interaction between the Pt nanoparticles and the graphene sheet with insufficient functional groups. However, covalently grafting either SO_3H− or NH_2− onto the graphene sheets could modify the surface chemical structure and provide more sites for anchoring the formed Pt nanoparticles. As a result, the majority of the Pt nanoparticles are able to retain their identical locations on the SO_3H-graphene and the NH_2-graphene after potential cycling. Location 3 (green circles in Figure 5c,d) shows that the change in the relative distance of the highlighted Pt nanoparticles, if any, on SO_3H-graphene is only 0.1 nm (from 7.1 to 7.0 nm). Similarly, Pt nanoparticles moved toward each other in location 4 by only 0.7 and 0.1 nm from 6.8 and 5.6 nm, respectively, on NH_2-graphene (location 4 in Figure 5e,f). Moreover, there are no obvious agglomerations detected in either case (Figure 5d,f), which underlines the strong interaction between the Pt and the supports with functional groups. Regardless, it has to be mentioned that the rate of particle coalescence is also dependent on the loading of particles on the supports.[46] However, during this IL-TEM study, Pt nanoparticles at a loading of 10 wt % were deposited on the gold grid in order to avoid overlapping particles that would affect the direct visualization. It is also noted that the sweeping potential ranges, cycle numbers, and electrolyte conditions (aerated or deaerated) would also affect the coalescence of Pt nanoparticles, causing the loss of ECSA and mass activity.[7b,47] To demonstrate the enhanced stability of Pt nanoparticles on functional graphene, graphene, SO_3H-graphene, and NH_2-

DOI: 10.1021/acscatal.5b02722
ACS Catal. 2016, 6, 2642−2653

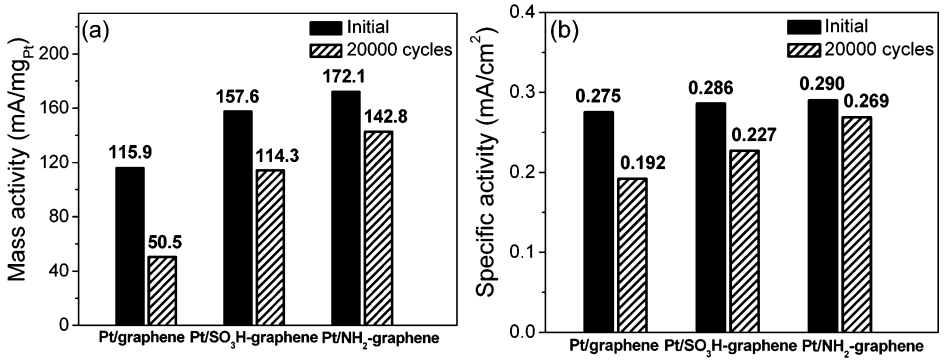

Figure 8. (a) Mass activity and (b) specific activity at 0.9 V vs RHE for Pt/graphene, Pt/SO_3H-graphene, and Pt/NH_2-graphene before and after 20000 cycles of ADT.

graphene supported Pt catalysts of 30 wt % loading were subjected to more harsh working conditions and compared in post-mortem TEMs.

TEM bright-field images of graphene, SO_3H, and NH_2 graphene supported Pt at 30 wt % loading are shown in Figure 6a,d,g. The results indicate that functional groups are able to help to improve the dispersion of the Pt nanoparticles regardless of the increase in the Pt loading, leading to a small average particle size and narrow size distribution of Pt/SO_3H-graphene (2.4 nm average particle size, ranging from 1 to 5 nm, Figure 6f) and Pt/NH_2-graphene (2.2 nm average particle size, ranging from 1 to 4 nm, Figure 6i). In sharp contrast, the aggregation of Pt nanoparticles with 30 wt % loading on the unmodified graphene became more severe than that with 10 wt % catalyst, where the majority of Pt particles were found joined together to become larger clusters at the crumpled regions of the graphene supports. The average particle size of Pt on graphene was about 3.5 nm with a wide size distribution from 1 to 8 nm (Figure 6c).

The electrocatalytic activity and the durability of functional graphene-supported Pt catalysts were studied on the rotating disk electrode (RDE). Cyclic voltammograms (CVs) collected in N_2-purged 0.1 M $HClO_4$ electrolyte are shown in Figure 7a,c,e. Upon integration of the Coulombic charge associated with the hydrogen desorption reaction from the potential between 0.05 and 0.4 V (vs RHE) in the CV curves,[48] the ECSA values for Pt/graphene, Pt/SO_3H-graphene, and Pt/NH_2-graphene were calculated to be 42.1, 55.1, and 59.3 m^2/g_{Pt}. The larger ECSA values obtained on Pt/SO_3H-graphene and Pt/NH_2-graphene suggest that the supported Pt nanoparticles are well exposed to the electrolyte, which originates from the better dispersed Pt nanoparticles with smaller sizes on both the SO_3H-graphene and the NH_2-graphene in comparison with those on graphene (Figure 6d,g vs Figure 6a). Improved dispersions of Pt nanoparticles on the functional graphene could also help to enlarge the space between graphene sheets that facilitate the diffusion of O_2 to access the Pt surface.[49] As a result, Pt/SO_3H-graphene and Pt/NH_2-graphene demonstrate excellent ORR activity, with mass activity at 0.9 V vs RHE of 157.6 and 172.1 mA/mg_{Pt}, respectively, which is superior to that of Pt/graphene (115.9 mA/mg_{Pt}) under the same testing conditions (Figure 8a). Accelerated degradation tests (ADTs) were then performed to study the stability of these electrocatalysts under potential-dynamic conditions. Tests were conducted by continuous sweeping of the potential between 0.6 and 1.0 V (vs RHE) at a scan rate of 100 mV/s for 20000 cycles. Figure 7a,c,e show that, the ECSAs of Pt/SO_3H-graphene and Pt/NH_2-graphene after the ADTs decreased to 50.3 m^2/g_{Pt} (91.3% retention) and 53 m^2/g_{Pt} (89.4% retention), respectively, while Pt/graphene underwent a significant decrease of ECSA to 26.3 m^2/g_{Pt} (62.5% retention). Meanwhile, ORR polarization curves recorded after 20000 cycles of ADT show that there are only 27 and 10 mV negative shifts in half-wave potentials and 27.5% and 17.0% loss of mass activity on Pt/SO_3H-graphene and Pt/NH_2-graphene, respectively (Figure 7d,f and Figure 8a). However, Pt/graphene exhibits a significant shift of half-wave potential by 53 mV and a loss of Pt mass activity by 56.4% (Figure 7b and Figure 8a). These results correspond to the 2.3 and 2.8 times higher mass activity of the Pt/SO_3H-graphene (114.3 mA/mg_{Pt}) and Pt/NH_2-graphene (142.8 mA/mg_{Pt}) in comparison to Pt/graphene (50.5 mA/mg_{Pt}) after ADTs, respectively (Figure 8a). In terms of specific activity, Pt/SO_3H-graphene and Pt/NH_2-graphene remain at 0.227 and 0.269 mA/cm^2 at 0.9 V vs RHE after ADT, respectively, which are higher than 0.192 mA/cm^2 on Pt/graphene (Figure 8b). Both functional graphene supported Pt demonstrated a smaller change of the specific activity (20.6% loss for Pt/SO_3H-graphene and 7.2% loss for Pt/NH_2-graphene) in comparison to Pt/graphene of 30.2% loss. These measured ORR activities agree well with the ECSA results, which indicate the improved activity and stability of the Pt nanoparticles as a result of the strengthened interaction between Pt and functional graphene. This not only leads to the uniform landing of the Pt nanoparticles but also prevents the Pt nanoparticles from growing into larger particles during the harsh ADTs.

Post-mortem TEM analysis was further used to characterize the degradation of the Pt nanoparticles on the different supports after 20000 cycles of ADTs. As shown in Figure 6e,h, there are few appreciable morphological changes for Pt/SO_3H-graphene or Pt/NH_2-graphene, where the Pt nanoparticles show distributions similar to those before the ADTs despite the average particle size slightly increasing from 2.4 to 3.5 nm for Pt/SO_3H-graphene and from 2.2 to 3.2 nm for Pt/graphene (Figure 6f,i). On the other hand, Pt/graphene demonstrates a dramatic increase in agglomeration; Pt nanoparticles agglomerated into large particles of irregular shapes. Specifically, Figure 6c shows that the average Pt nanoparticle size in Pt/graphene increased from 3.5 to 5.6 nm along with the particle size distribution moving toward a larger range of 2−10 nm after cycling. The coalescence of Pt nanoparticles on graphene adversely closes the gap between graphene sheets, causing a small decrease in the double-layer capacitance, as observed in Figure 7a. This further confirms the benefits of the functional

DOI: 10.1021/acscatal.5b02722
ACS Catal. 2016, 6, 2642−2653

groups, which can prevent migration, coalescence, and growth of the Pt nanoparticles to larger particles, all of which would sacrifice the ECSA and would be detrimental to the utilization and activity of Pt catalysts. Therefore, the results derived from this study show the promise of graphene surface functionalization for greatly improving the activity and durability of metal catalysts and is applicable in general catalysis realms.

CONCLUSIONS

In summary, we reported a facile preparation of *p*-phenyl SO_3H-graphene and *p*-phenyl NH_2-graphene as highly durable ORR catalyst supports for PEMFCs. The covalently grafted arylsulfonic or arylamino groups on the graphene surface with the respective diazonium compound produced in an aqueous phase are readily bonded on the $\pi-\pi$ conjugated honeycomb carbon network. The dispersion and the morphology of Pt on the unmodified graphene, SO_3H-graphene, and NH_2-graphene were characterized by HRTEM, and the stability of the supported Pt nanoparticles, when subjected to ADTs, was visualized using IL-TEM. During the deposition of Pt on graphene, functional groups that are uniformly bonded on the graphene surface clearly guide the nucleation and limit the agglomeration of Pt nanoparticles, which in turn leads to the reduced Pt nanoparticle size and narrow size distribution. The presence of functional groups prevents the migration of Pt nuclei on the 2-D graphene surface during both the nucleation and growth of the Pt nanoparticles and the dynamic electrochemical ADTs. The interaction between Pt nanoparticles and graphene supports was studied in detail using XPS and XANES. The results suggest that electrons withdraw from Pt and transfer to graphene carbons, and the S and N present in the functional groups serve to further stabilize the top layer of atoms in the Pt nanoparticles. This study sheds light on strategies to improve not only the durability but also the activity of Pt-based catalysts in fuel cells.

AUTHOR INFORMATION

Corresponding Author

*E-mail for J.X.: jianxie@iupui.edu.

Notes

The authors declare no competing financial interest.

ACKNOWLEDGMENTS

XAS was performed on Sector 20 facilities at the Advanced Photon Source, and research at these facilities is supported by the U.S. Department of Energy-Basic Energy Sciences, the Canadian Light Source and its funding partners, the University of Washington, and the Advanced Photon Source. Use of the Advanced Photon Source and the Center for Nanoscale Materials, Office of Science User Facility, operated for the U.S. Department of Energy (DOE) Office of Science by Argonne National Laboratory, was supported by the U.S. DOE under Contract No. DE-AC02-06CH11357.

REFERENCES

(1) Hickner, M. A.; Ghassemi, H.; Kim, Y. S.; Einsla, B. R.; McGrath, J. E. *Chem. Rev.* **2004**, *104*, 4587−4611.
(2) Antolini, E. *Appl. Catal., B* **2009**, *88*, 1−24.
(3) (a) Gasteiger, H. A.; Markovic, N. M. *Science* **2009**, *324*, 48−49. (b) Carrette, L.; Friedrich, K. A.; Stimming, U. *Fuel Cells* **2001**, *1*, 5−39. (c) Smith, W. *J. Power Sources* **2000**, *86*, 74−83.
(4) (a) Han, B.; Carlton, C. E.; Suntivich, J.; Xu, Z.; Shao-Horn, Y. *J. Phys. Chem. C* **2015**, *119*, 3971−3978. (b) Stamenkovic, V. R.; Fowler, B.; Mun, B. S.; Wang, G.; Ross, P. N.; Lucas, C. A.; Markovic, N. M. *Science* **2007**, *315*, 493−497. (c) Yano, H.; Kataoka, M.; Yamashita, H.; Uchida, H.; Watanabe, M. *Langmuir* **2007**, *23*, 6438−6445. (d) Paulus, U. A.; Wokaun, A.; Scherer, G. G.; Schmidt, T. J.; Stamenkovic, V.; Radmilovic, V.; Markovic, N. M.; Ross, P. N. *J. Phys. Chem. B* **2002**, *106*, 4181−4191. (e) Markovic, N. M.; Schmidt, T. J.; Stamenkovic, V.; Ross, P. N. *Fuel Cells* **2001**, *1*, 105−116.
(5) (a) Strasser, P.; Koh, S.; Anniyev, T.; Greeley, J.; More, K.; Yu, C.; Liu, Z.; Kaya, S.; Nordlund, D.; Ogasawara, H.; Toney, M. F.; Nilsson, A. *Nat. Chem.* **2010**, *2*, 454−460. (b) Srivastava, R.; Mani, P.; Hahn, N.; Strasser, P. *Angew. Chem., Int. Ed.* **2007**, *46*, 8988−8991. (c) Cui, C.; Gan, L.; Li, H.-H.; Yu, S.-H.; Heggen, M.; Strasser, P. *Nano Lett.* **2012**, *12*, 5885−5889. (d) Han, B.; Carlton, C. E.; Kongkanand, A.; Kukreja, R. S.; Theobald, B. R.; Gan, L.; O'Malley, R.; Strasser, P.; Wagner, F. T.; Shao-Horn, Y. *Energy Environ. Sci.* **2015**, *8*, 258−266.
(6) (a) Mazumder, V.; Chi, M.; More, K. L.; Sun, S. *Angew. Chem., Int. Ed.* **2010**, *49*, 9368−9372. (b) Gan, L.; Heggen, M.; Rudi, S.; Strasser, P. *Nano Lett.* **2012**, *12*, 5423−5430. (c) Karan, H. I.; Sasaki, K.; Kuttiyiel, K.; Farberow, C. A.; Mavrikakis, M.; Adzic, R. R. *ACS Catal.* **2012**, *2*, 817−824.
(7) (a) Borup, R.; Meyers, J.; Pivovar, B.; Kim, Y. S.; Mukundan, R.; Garland, N.; Myers, D.; Wilson, M.; Garzon, F.; Wood, D.; Zelenay, P.; More, K.; Stroh, K.; Zawodzinski, T.; Boncella, J.; McGrath, J. E.; Inaba, M.; Miyatake, K.; Hori, M.; Ota, K.; Ogumi, Z.; Miyata, S.; Nishikata, A.; Siroma, Z.; Uchimoto, Y.; Yasuda, K.; Kimijima, K.-i.; Iwashita, N. *Chem. Rev.* **2007**, *107*, 3904−3951. (b) Borup, R. L.; Davey, J. R.; Garzon, F. H.; Wood, D. L.; Inbody, M. A. *J. Power Sources* **2006**, *163*, 76−81.
(8) Gasteiger, H. A.; Kocha, S. S.; Sompalli, B.; Wagner, F. T. *Appl. Catal., B* **2005**, *56*, 9−35.
(9) (a) Xie, J.; Wood, D. L.; Wayne, D. M.; Zawodzinski, T. A.; Atanassov, P.; Borup, R. L. *J. Electrochem. Soc.* **2005**, *152*, A104−A113. (b) Xie, J.; Wood, D. L.; More, K. L.; Atanassov, P.; Borup, R. L. *J. Electrochem. Soc.* **2005**, *152*, A1011−A1020. (c) Shao-Horn, Y.; Sheng, W. C.; Chen, S.; Ferreira, P. J.; Holby, E. F.; Morgan, D. *Top. Catal.* **2007**, *46*, 285−305.
(10) (a) Chen, S.; Wei, Z.; Qi, X.; Dong, L.; Guo, Y.-G.; Wan, L.; Shao, Z.; Li, L. *J. Am. Chem. Soc.* **2012**, *134*, 13252−13255. (b) He, D.; Zeng, C.; Xu, C.; Cheng, N.; Li, H.; Mu, S.; Pan, M. *Langmuir* **2011**, *27*, 5582−5588.
(11) (a) Fujigaya, T.; Nakashima, N. *Adv. Mater.* **2013**, *25*, 1666−1681. (b) Yang, Z.; Berber, M. R.; Nakashima, N. *J. Mater. Chem. A* **2014**, *2*, 18875−18880.
(12) (a) Okamoto, M.; Fujigaya, T.; Nakashima, N. *Small* **2009**, *5*, 735−740. (b) Fujigaya, T.; Hirata, S.; Nakashima, N. *J. Mater. Chem. A* **2014**, *2*, 3888−3893.
(13) (a) Guo, L.; Jiang, W.-J.; Zhang, Y.; Hu, J.-S.; Wei, Z.-D.; Wan, L.-J. *ACS Catal.* **2015**, *5*, 2903−2909. (b) Chen, Y.; Wang, J.; Liu, H.; Banis, M. N.; Li, R.; Sun, X.; Sham, T.-K.; Ye, S.; Knights, S. *J. Phys. Chem. C* **2011**, *115*, 3769−3776. (c) Higgins, D.; Hoque, M. A.; Seo, M. H.; Wang, R.; Hassan, F.; Choi, J.-Y.; Pritzker, M.; Yu, A.; Zhang, J.; Chen, Z. *Adv. Funct. Mater.* **2014**, *24*, 4325−4336.
(14) Kou, R.; Shao, Y.; Mei, D.; Nie, Z.; Wang, D.; Wang, C.; Viswanathan, V. V.; Park, S.; Aksay, I. A.; Lin, Y.; Wang, Y.; Liu. *J. Am. Chem. Soc.* **2011**, *133*, 2541−2547.
(15) Matos, J.; Ono, L. K.; Behafarid, F.; Croy, J. R.; Mostafa, S.; DeLaRiva, A. T.; Datye, A. K.; Frenkel, A. I.; Roldan Cuenya, B. *Phys. Chem. Chem. Phys.* **2012**, *14*, 11457−11467.
(16) Behafarid, F.; Roldan Cuenya, B. *Surf. Sci.* **2012**, *606*, 908−918.
(17) Behafarid, F.; Ono, L. K.; Mostafa, S.; Croy, J. R.; Shafai, G.; Hong, S.; Rahman, T. S.; Bare, S. R.; Roldan Cuenya, B. *Phys. Chem. Chem. Phys.* **2012**, *14*, 11766−11779.
(18) Behafarid, F.; Roldan Cuenya, B. *Top. Catal.* **2013**, *56*, 1542−1559.
(19) (a) Zhang, B.; Su, D. S. *ChemCatChem* **2015**, *7*, 3639−3645. (b) Tauster, S. J. *Acc. Chem. Res.* **1987**, *20*, 389−394. (c) Campbell, C. T. *Nat. Chem.* **2012**, *4*, 597−598.

DOI: 10.1021/acscatal.5b02722
ACS Catal. 2016, 6, 2642−2653

(20) McAllister, M. J.; Li, J.-L.; Adamson, D. H.; Schniepp, H. C.; Abdala, A. A.; Liu, J.; Herrera-Alonso, M.; Milius, D. L.; Car, R.; Prud'homme, R. K.; Aksay, I. A. *Chem. Mater.* **2007**, *19*, 4396−4404.
(21) Li, D.; Kaner, R. B. *Science* **2008**, *320*, 1170−1171.
(22) Li, D.; Mueller, M. B.; Gilje, S.; Kaner, R. B.; Wallace, G. G. *Nat. Nanotechnol.* **2008**, *3*, 101−105.
(23) Rao, C. N. R.; Sood, A. K.; Voggu, R.; Subrahmanyam, K. S. *J. Phys. Chem. Lett.* **2010**, *1*, 572−580.
(24) Hummers, W. S.; Offeman, R. E. *J. Am. Chem. Soc.* **1958**, *80*, 1339−1339.
(25) Li, Z.-F.; Zhang, H.; Liu, Q.; Sun, L.; Stanciu, L.; Xie, J. *ACS Appl. Mater. Interfaces* **2013**, *5*, 2685−2691.
(26) Yu, K.; Groom, D. J.; Wang, X.; Yang, Z.; Gummalla, M.; Ball, S. C.; Myers, D. J.; Ferreira, P. J. *Chem. Mater.* **2014**, *26*, 5540−5548.
(27) Mayrhofer, K. J. J.; Ashton, S. J.; Meier, J. C.; Wiberg, G. K. H.; Hanzlik, M.; Arenz, M. *J. Power Sources* **2008**, *185*, 734−739.
(28) Dubau, L.; Castanheira, L.; Berthomé, G.; Maillard, F. *Electrochim. Acta* **2013**, *110*, 273−281.
(29) Higuchi, E.; Uchida, H.; Watanabe, M. *J. Electroanal. Chem.* **2005**, *583*, 69−76.
(30) (a) Si, Y.; Samulski, E. T. *Nano Lett.* **2008**, *8*, 1679−1682. (b) Li, Z.-F.; Xin, L.; Yang, F.; Liu, Y.; Liu, Y.; Zhang, H.; Stanciu, L.; Xie, J. *Nano Energy* **2015**, *16*, 281−292. (c) Xu, F.; Wang, M.-X.; Sun, L.; Liu, Q.; Sun, H.-f.; Stach, E. A.; Xie, J. *Electrochim. Acta* **2013**, *94*, 172−181.
(31) Park, S.; Hu, Y.; Hwang, J. O.; Lee, E.-S.; Casabianca, L. B.; Cai, W.; Potts, J. R.; Ha, H.-W.; Chen, S.; Oh, J.; Kim, S. O.; Kim, Y.-H.; Ishii, Y.; Ruoff, R. S. *Nat. Commun.* **2012**, *3*, 638.
(32) Malard, L. M.; Pimenta, M. A.; Dresselhaus, G.; Dresselhaus, M. S. *Phys. Rep.* **2009**, *473*, 51−87.
(33) Das, A.; Chakraborty, B.; Sood, A. K. *Bull. Mater. Sci.* **2008**, *31*, 579−584.
(34) Ni, Z. H.; Wang, H. M.; Ma, Y.; Kasim, J.; Wu, Y. H.; Shen, Z. X. *ACS Nano* **2008**, *2*, 1033−1039.
(35) Eigler, S.; Grimm, S.; Enzelberger-Heim, M.; Muller, P.; Hirsch, A. *Chem. Commun.* **2013**, *49*, 7391−7393.
(36) (a) Paulus, G. L. C.; Wang, Q. H.; Strano, M. S. *Acc. Chem. Res.* **2013**, *46*, 160−170. (b) Lomeda, J. R.; Doyle, C. D.; Kosynkin, D. V.; Hwang, W.-F.; Tour, J. M. *J. Am. Chem. Soc.* **2008**, *130*, 16201−16206.
(37) Meyer, J. C.; Geim, A. K.; Katsnelson, M. I.; Novoselov, K. S.; Booth, T. J.; Roth, S. *Nature* **2007**, *446*, 60−63.
(38) Stankovich, S.; Dikin, D. A.; Piner, R. D.; Kohlhaas, K. A.; Kleinhammes, A.; Jia, Y.; Wu, Y.; Nguyen, S. T.; Ruoff, R. S. *Carbon* **2007**, *45*, 1558−1565.
(39) Volmer, M.; Stratmann, M.; Viefhaus, H. *Surf. Interface Anal.* **1990**, *16*, 278−282.
(40) Zhang, J.; Zhao, Z.; Xia, Z.; Dai, L. *Nat. Nanotechnol.* **2015**, *10*, 444−452.
(41) Kuo, P.-L.; Chen, W.-F.; Huang, H.-Y.; Chang, I. C.; Dai, S. A. *J. Phys. Chem. B* **2006**, *110*, 3071−3077.
(42) Cheng, N.; Norouzi Banis, M.; Liu, J.; Riese, A.; Mu, S.; Li, R.; Sham, T.-K.; Sun, X. *Energy Environ. Sci.* **2015**, *8*, 1450−1455.
(43) Mukerjee, S.; Srinivasan, S.; Soriaga, M. P.; McBreen. *J. Electrochem. Soc.* **1995**, *142*, 1409−1422.
(44) Ankudinov, A. L.; Rehr, J. J.; Low, J. J.; Bare, S. R. *J. Chem. Phys.* **2002**, *116*, 1911−1919.
(45) Miller, J. T.; Schreier, M.; Kropf, A. J.; Regalbuto, J. R. *J. Catal.* **2004**, *225*, 203−212.
(46) Meier, J. C.; Galeano, C.; Katsounaros, I.; Topalov, A. A.; Kostka, A.; Schüth, F.; Mayrhofer, K. J. J. *ACS Catal.* **2012**, *2*, 832−843.
(47) Shao, Y.; Yin, G.; Gao, Y. *J. Power Sources* **2007**, *171*, 558−566.
(48) Arenz, M.; Mayrhofer, K. J. J.; Stamenkovic, V.; Blizanac, B. B.; Tomoyuki, T.; Ross, P. N.; Markovic, N. M. *J. Am. Chem. Soc.* **2005**, *127*, 6819−6829.
(49) Si, Y.; Samulski, E. T. *Chem. Mater.* **2008**, *20*, 6792−6797.

DOI: 10.1021/acscatal.5b02722
ACS Catal. 2016, 6, 2642−2653